

Electron Positron Annihilation

Mähring, Marcus

February 13, 2021

Abstract

In this experiment, the β^+ decay of a ^{22}Na sample is examined using Nuclear Instrument Modules (NIMs) and an oscilloscope. After determining some features of the equipment, the decay's energy spectrum was recorded using an SCA and then an MCA card both with and without coincidence. The author could then identify the components of the decay scheme in the spectra, as well as find which effects appear in coincidence with one another. Next, the Compton edges and photopeaks from theory were identified and used as an energy calibration by using the theoretical energies of the features. From this, the detector was determined to be non-linear an odd outlier at about 850 keV. Meaning the detector most probably exhibits some saturation in this area. Finally, the unidentified structure in the spectra was found to correspond to remnants of electron capture in the sample and backscattering close to the Compton edge.

Contents

1	Introduction	4
1.1	Goals of the experiment	4
1.2	The annihilation process	4
1.3	Photon-matter interaction	5
1.4	Detecting the decay	6
2	Experiment	8
2.1	Equipment	8
2.1.1	The NIM crate	8
2.1.2	The source	9
2.2	Initial observations, detector fluorescence, and saturation	10
2.2.1	Initial observations and detector fluorescence	10
2.2.2	Saturation	10
2.3	Determining the working point for the PMT	11
2.4	Integrated spectrum with a SCA and a scalar	12
2.5	Spectrum with MCA card without coincidence	13
2.6	Observing decay with coincidence	13
3	Results	16
3.1	Saturation	16
3.2	Working point of the PMT	16
3.3	Manual integrated spectrum with SCA	18
3.4	MCA without coincidence and energy calibration	19
3.5	MCA spectrum with coincidence	19
4	Discussion	21
4.1	Analysis of initial observations	21
4.1.1	More present line in spectrum	21
4.1.2	Fluorescence of NaI(Tl)	21
4.2	Working point of PMT	23
4.3	Manually integrated spectrum with SCA	23
4.4	MCA without coincidence	24
4.4.1	Feature recognition	24
4.4.2	Feature fitting	25
4.4.3	Energy calibration	29
4.4.4	Identification of lower peak and comparison with MCA without coincidence	31
4.5	MCA spectrum with coincidence	33

5	Conclusion	35
A	Safety considerations	36
A.1	The activity of the Na source	36
A.2	Protection by shielding	37
A.3	Average dose	39

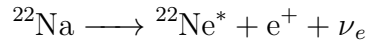
1 Introduction

1.1 Goals of the experiment

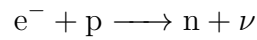
This experiment aims to introduce the author to some methods and tools used in some nuclear physics research as well as investigate the (β^+) -decay of a ^{22}Na sample. Positron decay has become more and more important being both used in medicine (Positron Emission Tomography - PET) and being a fundamental interaction in quantum electrodynamics.

1.2 The annihilation process

The simplified process is as follows: emitted positron quickly scatters in the medium, inducing an annihilation between the positron and the electron.

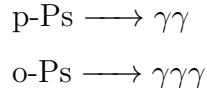


Where $^{22}\text{Ne}^*$ is an excited state of neon, which falls back to its ground state, producing a photon with energy 1.275 MeV. In actuality, a short lived bound state called *positronium*, which in turn decays into 2γ or 3γ [1]. The above process describes the positron decay, but additionally about 10% of the decay is due to electron capture, a process where an electron from the shell (mostly the K shell, but sometimes the L shell with a lower probability) fuses with a proton in the nucleus expelling a neutron and a neutrino [2]:



This transition is almost impossible to detect directly due to neutrinos being difficult to detect [3]. However, the electron capture leaves a hole in the shell which gets filled by another electron, giving rise to an emission of a x-ray [2].

The decay of the positronium is determined by considering the spin state of the electron-positron pair. We label them *ortho-positronium*, o-Ps – a triplet spin state with parallel spins – and *para-positronium*: p-Ps, singlet state with anti-parallel spins. They obey the following decays to conserve the total spin:



If one considers the momentum conservation in these decays it follows immediately, that the p-Ps decay must happen so that the momenta of each photon have equal magnitude but are opposite. Analogously, from energy conservation it holds that each photon has energy equal to the electron rest mass: ~ 511 keV. The o-Ps state has a multipole configuration, providing additional stability, where o-Ps has a lifetime of 1.42×10^{-7} s in vacuum, significantly longer

than p-Ps at 1.25×10^{-10} s [1]. In practice, this experiment will only focus on the p-Ps decay as o-Ps decay occurs much less frequently.

1.3 Photon-matter interaction

Photons interact with matter distinctly different to charged particles, as they loose energy through a gradual process interactions with the material. There are three main kinds of interactions for the photons: *photoelectric absorption*, *Compton scattering*, and *pair production* [1][4].

Photoelectric absorption describes the interaction of a photon with an atomic electron, leading to the absorption of the photon and the excitation of the atom. Let E_γ be the energy of the photon, then the electron gets the kinetic energy:

$$E_e = E_\gamma - E_b$$

Where E_b is the binding energy of the ejected electron. This can only happen with bound electrons, as such an interaction with a free electron would violate the conservation of momentum.

Compton scattering describes the scattering of photons on electrons, leading to an energy transfer to the electron and a deflection mirrored from its initial approach. The electron gains the energy:

$$E_e = E_\gamma - E'_\gamma$$

with E'_γ being the energy of the reflected atom. It can be shown that this quantity obeys the relation:

$$E'_\gamma = \frac{E_\gamma}{1 + \frac{E_\gamma}{m_e c^2} (1 - \cos \theta)} = E_\gamma \cdot P(E_\gamma, \theta)$$

Here $P(E_\gamma, \theta)$ describes the ratio of photon energy before and after the scattering. The rest mass of the electron, $m_e c^2 \approx 511$ keV will reappear throughout this report. As incident angle of the photon is arbitrary, θ varies from 0 to π radians. When θ goes to zero, no energy is transferred.

The amount of photons observed at the different scattering angles, and corresponding electron energies is given by the Klein-Nishina scattering formula which follows from quantum electrodynamics [2]:

$$\frac{d\sigma}{d\Omega} = \frac{1}{2} \alpha^2 r_c^2 P(E_\gamma, \theta)^2 [P(E_\gamma, \theta) + P(E_\gamma, \theta)^{-1} - \sin^2 \theta] \quad (1)$$

Here α is the fine structure constant and $r_c = \hbar/m_e c$ the reduced Compton wave-length [2].

In our case, E_γ is equal to the rest mass of the electron, $m_e c^2$ for the p-Ps decay and $\frac{2}{3} m_e c^2$ for the o-Ps decay. Additionally at $\theta = \pi$ backscattering is going to take place, we get an

energy of $E'_\gamma = \frac{E_\gamma}{3} = 170 \text{ keV}$. At this point we also find the Compton edge, the point where the most photons are scattered, before the amount of scattered photons quickly drops (see (1)). Here the maximum energy acquired by the electron is $E_e = \frac{2}{3}E_\gamma = 340 \text{ keV}$ [1]. Note that one may substitute E_γ for any arbitrary Compton backscattering emission one wishes to study.

The pair production mechanism describes the creation of an electron, positron pair from a photon, with energy $\geq 2m_e c^2 = 1.022 \text{ MeV}$, though this mechanism is negligible for energies smaller than several MeV [1].

1.4 Detecting the decay

Ultimately, the visibility of the different mechanisms is determined by the scattering cross section of the electrons with the material in the scintillator used. The scintillator absorbs energy from the high-energy incoming radiation and converts the absorbed energy to lower energy photons, which in turn generate current in the PMT. The attenuation coefficient of the type of scintillator used in the experiment (NaI(Ti)) is given in figure 1.

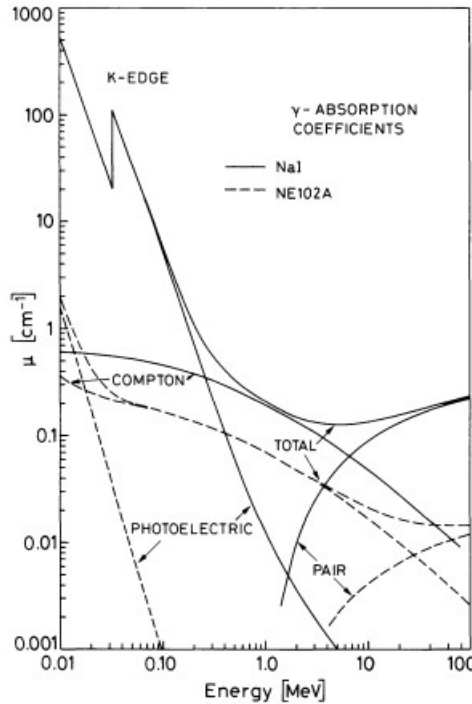


Figure 1: The attenuation coefficient plots of a NaI(Ti) scintillator as well as a typical plastic scintillator (NE102A). Additionally, the contributions from the individual effects are marked in the respective regions where applicable [2].

In our experiment, both the photoelectric and Compton effects have a significant cross section and as such we expect both to appear during the course of the experiment [1]. An example of this spectrum is shown in figure 2.

In practice, the sharp peaks and transitions seen in figure 2 are emblematic of a detector

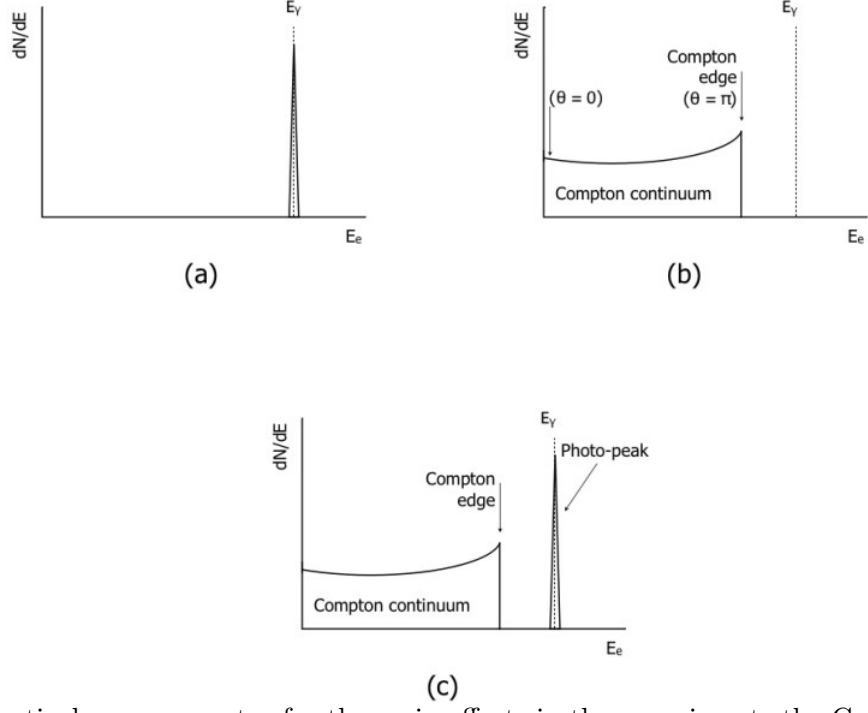


Figure 2: Theoretical energy spectra for the main effects in the experiment: the Compton edge and photopeak. In the above two parts, the structure of these features are shown individually and then lower part shown together [1].

with a perfect to very high energy resolution. The detector used in this experiment, a NaTi scintillator, has a lower resolution and will thus induce smearing in the peaks and edges. Specifically, the energy resolution – which shall be determined during the experiment – can be approximated by determining the Full Width Half Maximum (FWHM) of its peaks:

$$R_{\text{FWHM}} = \frac{\Delta E}{E} \stackrel{\text{Gaussian}}{=} \frac{2.35\sigma}{E} \quad (2)$$

Meaning if a Gaussian is fit to a peak in the spectrum, the quotient of the found standard deviation with its mean (if normalized) provides a value proportional to the energy resolution [5][6].

As mentioned above, the experiment employs the use of NaI(Ti) scintillators, which are preferential over for instance NE102A as it has a significantly higher detection rate in domains where photoelectric effects as well as pair production dominate. Especially the photoelectric effect is essential in γ -measurements, as it produces the characteristic photopeak, making the NaI(Ti) scintillator the clear choice.

2 Experiment

2.1 Equipment

2.1.1 The NIM crate

In this experiment a Nuclear Instrumentation Module (NIM) crate is used. This is a housing in which several digital/analogue signal processing modules may be installed. It is usually characterized by being an exceptional grounding. It usually allows for both digital and analogue signals. For digital signals one voltage is conventionally set to assign the logical false to 0 V and the logical true to some voltage. In the case of a NIM signal, it is actually current based with the zero ("false") set to 0 mV and true set to -16 mA (which when fed through a $50\ \Omega$ resistor corresponds to -0.8 V). Some modules used in this experiment are now presented with a short explanation of their functionality.

High voltage source (HV) to produce the high voltages needed in the photomultipliers, which are responsible for amplification of the signal.

Two photomultipliers (PMTs) were used in the experiment. They work by taking the photoelectrons produced from the scintillator photons and from the initial electron creating a cascade of subsequent electrons, amplifying the signal (see figure 3). They allow for the output of an analogue signal (entire collected signal) with positive polarity which undergoes some pre-processing as well as the dynode which has no pre-processing with a fast rise time.

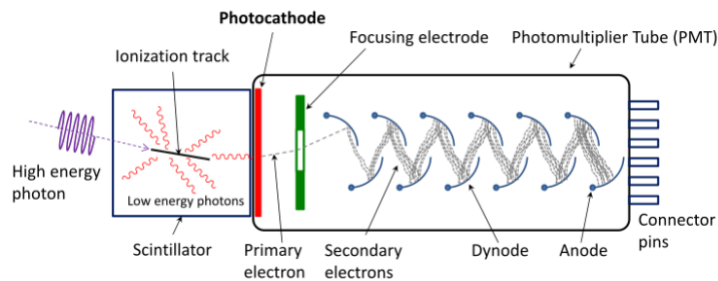


Figure 3: A schematic describing the use of a scintillator together with a PMT. First a photon or charged particle enters the scintillator and is subsequently transformed into low energy photons through interaction with the scintillator material. These are in turn converted into primary electrons using a photocathode which are then fed to the PMT amplifying the signal [7].

Fan in fan out is a simple module which copies the incoming pulse (in the experiment, a linear one is used, meaning it accepts both analogue and digital signals) into several identical pulses.

A discriminator is a unit which takes an input signal and only outputs a digital signal if the amplitude of the input exceeds a certain value. The threshold of the input and the width of the signal can be adjusted mechanically on the discriminator which also includes an output such that the threshold can be read using a multimeter.

The dual timer delay trigger (D.TRIG) is a unit working with digital signals both as input and output. It has two independent time parameters, delay and width. The width specifies the width of the output signal while the delay determines the delay from a received signal to the output of the new signal. It only takes NIM signals but outputs both TTL and NIM signals.

Single channel analyzer (SCA) is a discriminator which compares the input signal with an upper as well as a lower bound. It takes an analogue signal and outputs a logical (digital) true if the analogue signal falls within the set range. In this experiment it is used with a scalar, which counts the amount of received signals within a set time frame.

The coincidence unit determines if two signals are coincident in time and generates a logical signal if this is true. The signal is of a constant width and can be set manually.

Additionally, an oscilloscope to image the produced signals was used. During the entire experiment the signals were always terminated at the scope with a total resistance of $50\ \Omega$. Mostly this comes from an explicit termination with a resistor but sometimes the resistance is implicitly included in the output from the NIM crate. This is done to prevent the signal from reflecting at the termination of the translation line. Reflection can cause distortion and ambiguous levels [8].

2.1.2 The source

The source used is a ^{22}Na source acquired in April 2009. In appendix A.1 the present activity is determined to be $(13.21 \pm 0.18)\text{ kBq}$. Additionally, safety considerations are discussed. However, it is still of great interest to determine the expected count rate of the detector, of which the setup can be seen in figure 4. The area of a detector with a diameter of 2.54 cm

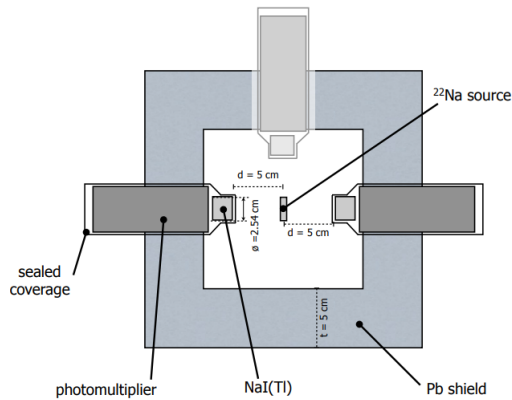


Figure 4: A sliced view of the ^{22}Na source together with some essential dimensions of the setup. Note the shielding and how the detectors are mounted such that they do not break this seal considerably [1].

has the area $A_{\text{Source}} = \pi(d/2)^2$ with d the diameter of the detector, $d = 25.4\text{ mm}$. We assume the decay of the sample is isotropic and the detector is at a distance of $r = 5\text{ cm}$ from the

detector. Meaning we get the following average detected activity:

$$\bar{N}_{\text{Detected}} = \frac{\pi \cdot (d/2)^2}{4\pi r^2} N = \frac{d^2}{16r^2} N = (213.0 \pm 2.8) \text{ Bq} \quad (3)$$

Over the 10 s measuring time we subsequently expect about (2130 ± 28) events, assuming perfect detection efficiency, meaning we expect about three times that amount of photons with two being spatially correlated. If one assumes the particle travels a distance of 25.4 mm in the scintillator, and assuming two photons have energy 511 keV and one has energy 1275 keV from figure 1 one gets a linear attenuation of about 0.3 cm^{-1} and 0.13 cm^{-1} . Using Beer-Lambert's law (appendix A.2) we linearly add the contributions from the 511 keV and 1275 keV photon contributions. Using $1 - T$ for absorption instead of transmission, one subsequently should expect about (994 ± 13) Bq counts over a ten second interval. Note that this does not account for contributions from the o-Ps decay.

2.2 Initial observations, detector fluorescence, and saturation

2.2.1 Initial observations and detector fluorescence

Before starting the experiment, the high voltage cables needed to be connected to the PMT. This was done by first connecting a high-voltage cable to the HV source and then to a 1/1000 voltage divider. This was in turn wired to an Ohm-meter, where voltage was shown in volts, but due to the voltage divider it corresponded to the displayed value in kilo volts. Then a HV cable was wired from the output of the divider to the PMT.

For the initial observation of the signal, first the voltage was set to 800 V. Then, the anode output was connected to the oscilloscope (scope) and terminated with $50 \text{ m}\Omega$. The time scale was set to 250 ns/div and the scale of the voltage was set to 500 mV triggering at a 50 mV threshold with 5 s persistence on the scope. From this point out, the signal could be imaged on the screen.

The above steps were repeated for the dynode signal with a time scale of 100 ns and voltage of 100 mV . From this signal the fluorescence time of the NaI(Tl) shall be determined in a later stage.

2.2.2 Saturation

In this step, the valid range of the PMT, to avoid saturation, was found. The voltage at which saturation occurs is where the signal is maximized. Meaning for any voltage above this value, several photon energies will be perceived as the same energy by the experiment, as the signal post PMT will look identical. For our PMT, which is custom-designed at ETH, an indication of saturation is when above the normal anode signal additional structure in the form of additional lines and or bumps on the graph appear 6. As such several stills were made at different voltages ranging from 1200 V and 900 V .

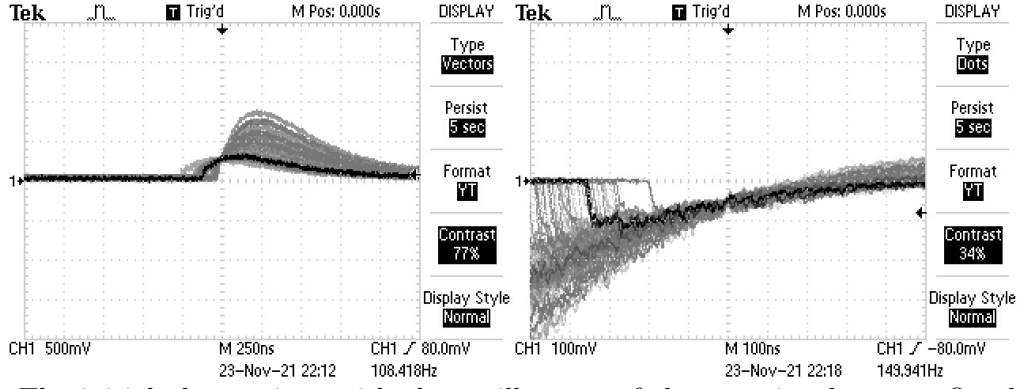


Figure 5: The initial observations with the oscilloscope of the two signal types. On the left the anode is displayed and the dynode on the right. In the dynode signal, some parts are obscured as the author had not yet learned how to correctly use the scope.

From the recorded stills from the oscilloscope the point of saturation was determined to be about 910 V, meaning the experiment should be performed below this voltage.

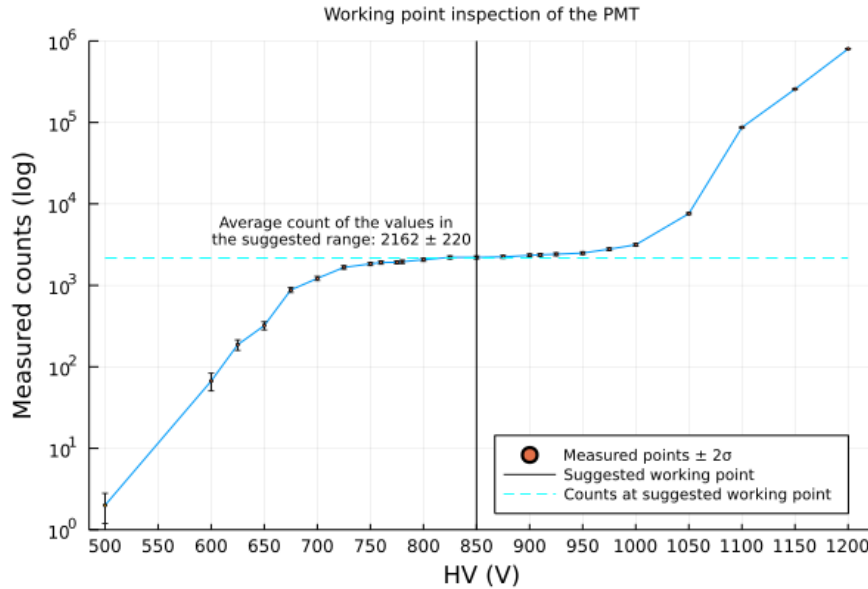


Figure 6: Recorded count values for different bias voltages. Additionally the determined working point is given.

2.3 Determining the working point for the PMT

Another note when working with the PMT is that one needs to find the high voltage range where the gain (amplification of the signal) is significant, letting as much of the signal in as possible, while not reaching a region where noise from the electronics add counts. We thus expect a rising region where not enough of the signal is let through, a plateau region where the counts are relatively stable, and finally a region where noise starts to add to the counts. We wish to determine the voltages which specify the plateau region.

To this end a simple circuit was constructed, outputting the dynode from the PMT leading to a fan-in fan-out module to split the signal. One output from that was directly connected to the scope, while another output was connected to the discriminator with a threshold of

50 mV. From the discriminator – outputting a NIM signal – one output was wired to the trigger of the oscilloscope and another to the D.TRIG module.

The D.TRIG module is here to ensure that one signal does not get counted several times, as this would artificially inflate the counts, leading to a systematic error. To this end, the D.TRIG is used to produce a longer output which was then tuned to ensure that per discriminator-processed dynode signal, only one gets counted. The delay was set to 1 μ s. Thereafter, a scalar was connected to the D.TRIG output. This entire setup can be seen in figure 7.

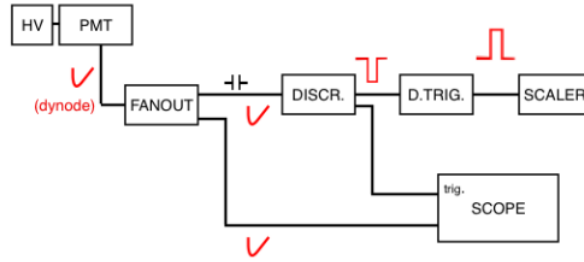


Figure 7: The circuit configuration for determining the working point of the PMT. Note how every signal is a dynode signal except the logical output from the D.TRIG signifying if a count should be recorded. [1]

The voltage range from 0 to 1200 was swept in increments of about 50 V, but in some parts of the range where the count difference was low, a step size of 100 V was sometimes employed. Likewise, in areas of interest the step size used was 25 V. A voltage of 850 V was decided upon from the results of the measurement.

2.4 Integrated spectrum with a SCA and a scalar

In this step the energy spectrum of the ejected γ radiation was measured. In the first step, it was done by using a SCA in window (ΔE) mode, to sweep a range of different voltages of the signals from the PMT; the voltages correspond to the energies of the γ -rays. In figure 8 a diagram of the setup is given. On the SCA, we change the Lower Level Discriminator (LLD) in increments of ΔE , meaning for every LLD value we scan the range $[LLD, LLD + \Delta E]$, giving an indication of the amount of counts in the given range.

As shown in Figure 8 the anode output of the PMT was connected to the PMT. Then from the SCA the S.C.A output was used as the trigger for the scope as well as for the scalar. Additionally, the BLR output from the scope was imaged on the scope. The aforementioned connection was not explicitly terminated at the scope, but was implicit in the module.

First, a general sweep was performed with a $\Delta E = 200$ mV with non-equidistant LLD values in steps between 0.01 V and 0.5 V to create an intuitive understanding of the general structure of the spectrum. The counts were measured during a 10 s time interval. The measurement was repeated using a window size of 50 mV sampling at equidistant points incrementing by

the window size. Both measurements were carried out in the range from circa 0 to 2.5 V. These measurements were carried out with 20 s of count-time. The results from this can be seen in Figure 14.

2.5 Spectrum with MCA card without coincidence

Next, the previous measurement was repeated using an integrated Multi-Channel Analyzer (MCA) card. The MCA converts the amplitude of the incoming analogue signal into a digital signal and automatically generates a histogram of the data.

To setup the measurement the analogue output was directly connected to the leftmost connection of the MCA (the input). The MCA results were displayed in corresponding MC3A software disabling the gate option for the MCA (otherwise no signals would be recorded) and a range of 4096 bins were chosen. The lower level ADC was set to 0.002 V. The spectrum was recorded for three hours and 46 minutes.

In this way the MCA resembles the SCA but with a small bin size (0.002 V) and a high amount of bins (4096).

2.6 Observing decay with coincidence

In this final measurement, the decay of the source was observed with a secondary detector to only observe events coincident in time, meaning we should only observe the remnants from the p-Ps decay.

To this end the second scintillator vis-à-vis the first was wired to the HV with the same configuration with a voltage divider and multimeter as the first PMT and both were set to 850 V. Then the circuit in Figure 9 was set up as described below.

The circuit consists of a few distinct parts. The first most obvious connection, is that the anode needs to be connected to the MCA input, however, in a later stage we will see that we might need to impose a delay on this signal for it to match the logical signal from the rest of the circuit.

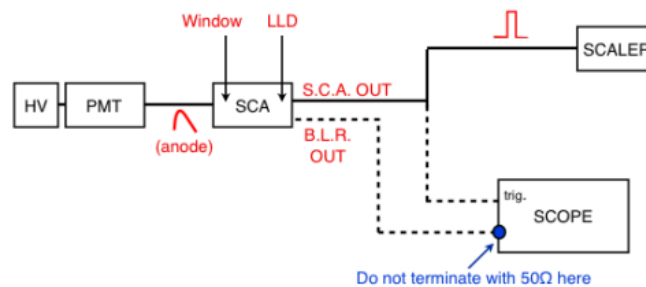


Figure 8: Circuit configuration for the integrated spectrum using the SCA. Again a TTL signal goes to the scaler. Note that BLR output already has an integrated 50 Ω resistor, meaning that termination is not needed.

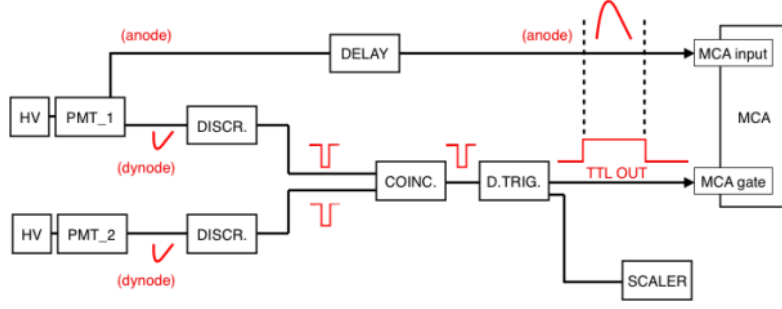


Figure 9: Circuit schematic for the MCA observation. The above part with just the anode signal being connected to the MCA card corresponds directly to the circuit used in section 2.5. Note how the circuit also indicates the coincidence of the anode signal [1].

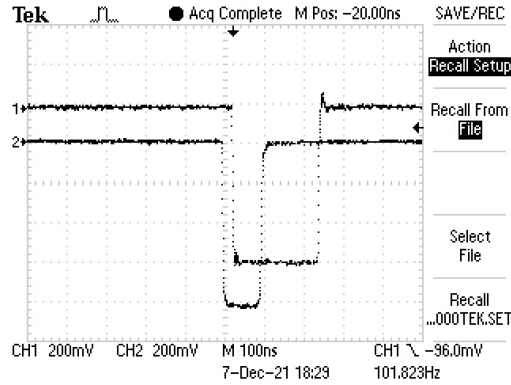


Figure 10: An example of the coincidence and discriminator output. Note the small displacement in time which the signals carry; this is one place where the delay of the equipment and the cables leads to a difference which needs to be counteracted for the coincidence to work.

In a first stage, both dynode outputs from the PMTs were connected to a discriminator with a threshold of 50 mV each. The output NIM signals were then wired to the coincidence unit. The wiring up to this point lead to a relative delay between the two dynode outputs of 2 ns. The output of the scope was imaged first together with the output of one discriminator and then with the other to ensure that they were indeed generating a coincidence and that the discriminator outputs were realistic, see figure 10.

The coincident signal was the connected to the D.TRIG, whose output will serve as the gate for the MCA measurement. An important factor here, as mentioned before, is that the TTL signal from the D.TRIG and the anode signal must arrive at the MCA card at the same time, otherwise only the overlap between the max and analogue would be used, instead of measuring the entire signal.

To ensure this coincidence, the D.TRIG output and the anode signal were imaged on the scope. Then the delay on the anode and from the D.TRIG were adjusted until the signals were overlapping in time. No additional delays were added on the D.TRIG line. However, for the anode signal 72 ns¹ were added to ensure the signal lay within the logical signal. The ultimate result can be seen in figure 11.

¹66 ns worth of delay were added using the delay module and an additional 6 ns from wires

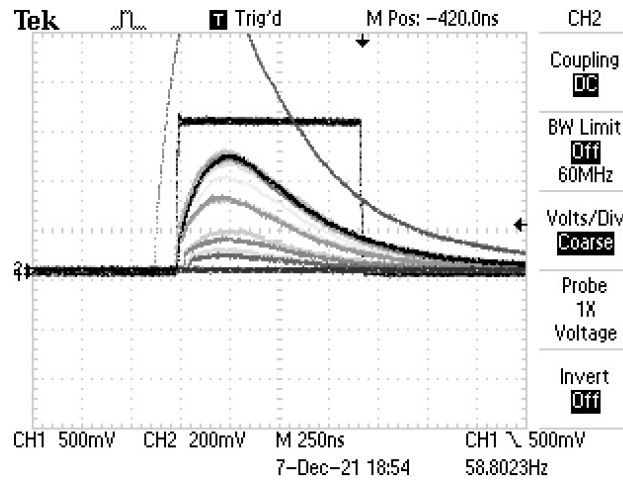


Figure 11: The anode signal overlaid on top of the D.TRIG output. Note how they are coincident in time even though the D.TRIG signal has had a much greater delay applied to it. This is thanks to the delay applied to the anode signal.

Before recording the final spectrum with coincidence, the count rate was once again measured with the scalar both with the logical signal limiting the counting to coincidence, and again switching both PMT signals in the coincidence unit; this was done one PMT at the time.

3 Results

3.1 Saturation

In image 12 the anode signals for 900 V and 975 V imaged at 5 s and infinite persistence (in actuality, the infinite imaging was close to 5 s as well). Note additional bulging of the curve on the right as well as the additional streaks above the normal curve. This indicates saturation and especially the bulging becomes a valuable source of information as the streaking only appears for some higher voltages.

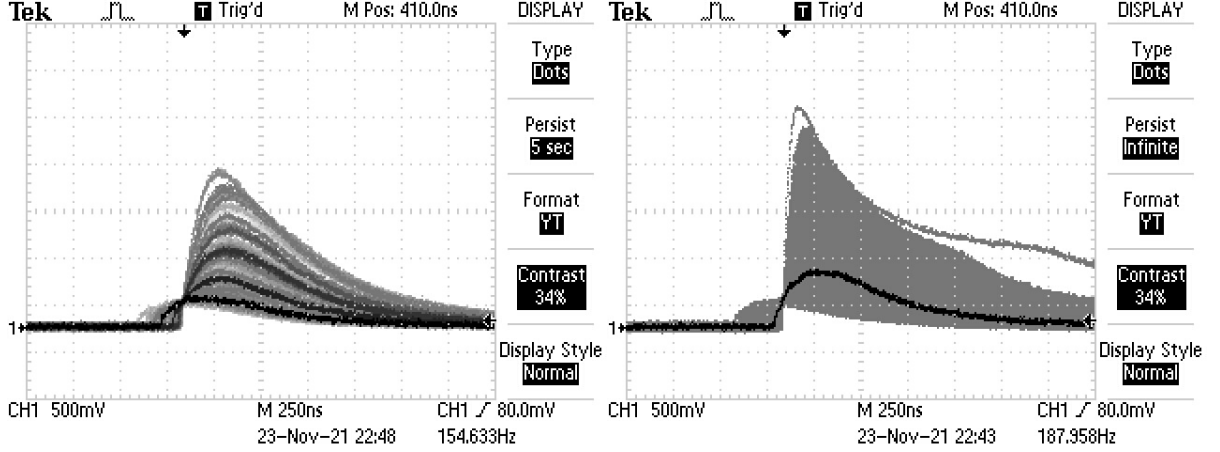


Figure 12: Two examples of anode curves. On the right (900 V bias) little saturation is observed with the curve keeping its shape while on the right (975 V) heavy saturation occurs with an additional bulge and tearing of the curve.

With this in mind, the voltages especially around 900 V were sampled. Subsequently it was found that while the signals at 900 V exhibited no clear bulging, at 905 V it started to appear and at 910 V it became noticeable. One image taken at this voltage can be seen in figure 13 with some noticeable bulging overlaying the right part of the curve (in relation to the middle).

3.2 Working point of the PMT

In figure 6 a graph of a subset of the recorded points from measuring the count rates for different voltages is displayed. These points were chosen because they most aptly captured the expected shape of the saturation count curve from [1]. From the consideration that the curve should be as flat as possible, the working point of 850 V was chosen as it was the inflection point of the graph.

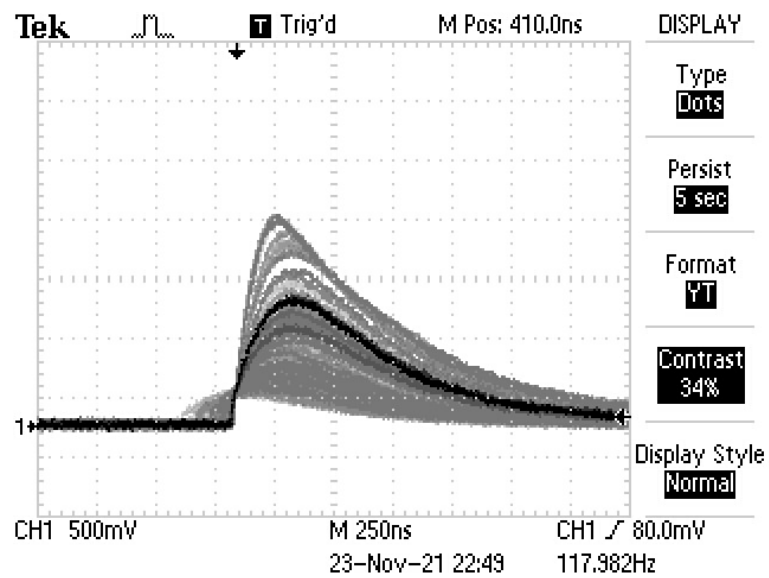


Figure 13: The cutoff point from which saturation started to become noticeable. Observe how in the two boxes right from the middle, additional bulging can be seen.

3.3 Manual integrated spectrum with SCA

From the integrated spectra, two histograms were created. In figure 14 these are shown. On the left in the figure one finds the initial spectrum made to get a sense of the equipment and the spectrum, and on the right the precision spectrum at (50 ± 3) mV. The experiment is a so-called counting experiments, counting decays of a radioactive source. Here the average decay time of the sample is much shorter than the expected half-life of the sample, justifying the use of Poisson statistics for analyzing the data. For a Poisson distribution we have $\mu = \lambda$, with λ being the expected counts. Thus the standard deviation in a counting experiment should follow $\sigma = \sqrt{\lambda} = \sqrt{N}$.

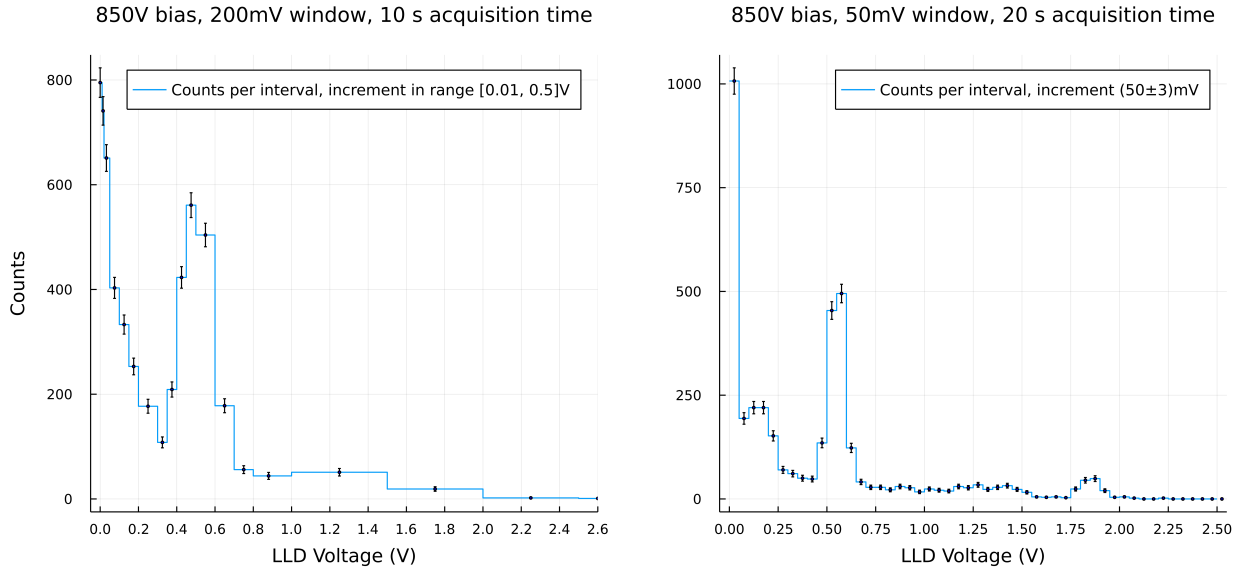


Figure 14: Two energy spectra (given in terms of voltage) for different SCA window sizes with the left one having bigger windows varying between 0.01 and 5 V while the right one is kept fixed.

Here one can clearly see indications of some structure, especially in the sampling with a smaller step size with clear peaks at about 0.5 V and a resemblance of a peak at around 1.75 V.

3.4 MCA without coincidence and energy calibration

In figure 15 the same spectrum as before recorded over 3 hours and 46 minutes is shown. On the x-axis the ADC (Analogue to Digital converter) channel, meaning we are converting the anode signal into some digital value. This x-axis may be calibrated to represent the energy of the recorded photon.

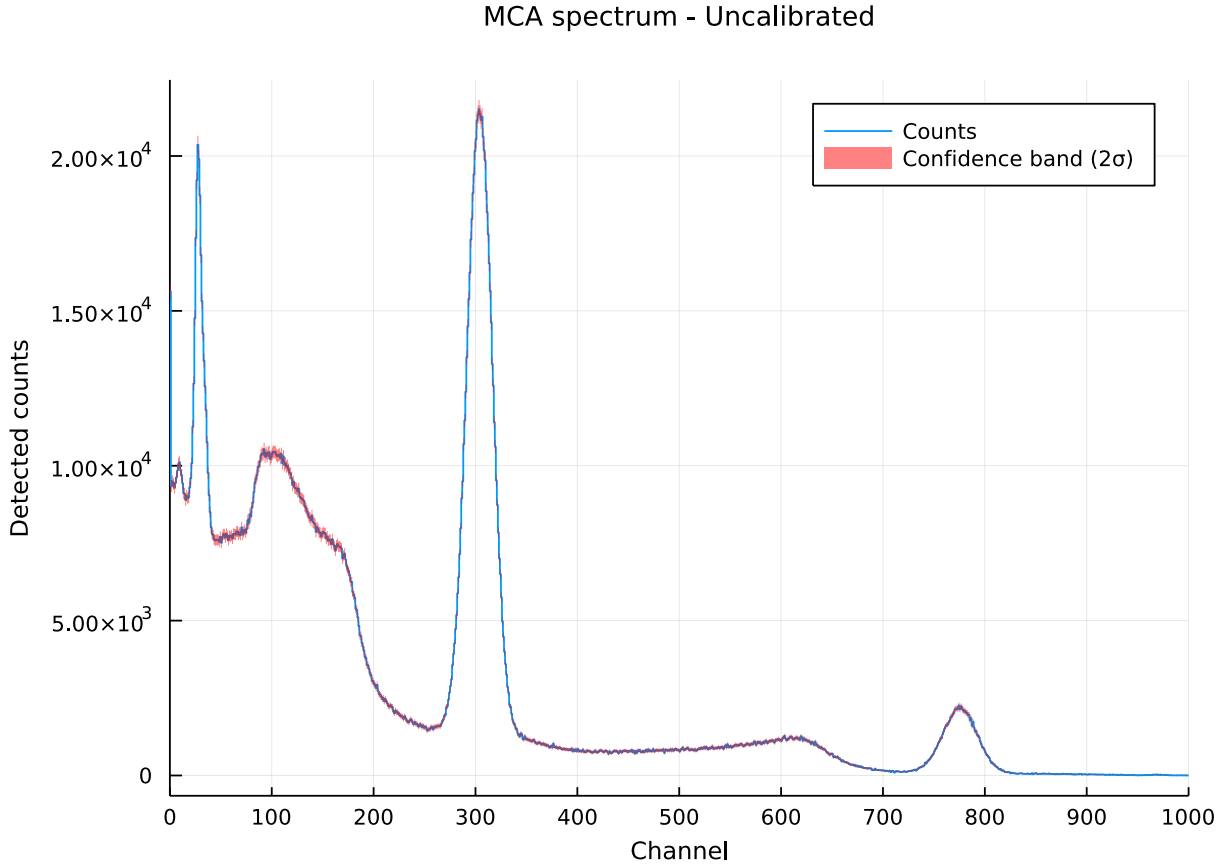


Figure 15: The recorded, uncalibrated, MCA spectrum without coincidence marked with the Poisson error along the curve.

3.5 MCA spectrum with coincidence

For the MCA with coincidence and calibration, its curve is displayed in figure 16. Note the blue band about the central red line indicating two standard deviations. In figure 17 the logarithm of counts displayed in the the above plot is depicted.

The counts recorded with coincidence was about 600, while when turning off the coincidence module again gave values in the range of ~ 2300 counts. The differences to the originally observed counts, the explicit measured values, and how they compare to the expected counts will be discussed in 5.5.

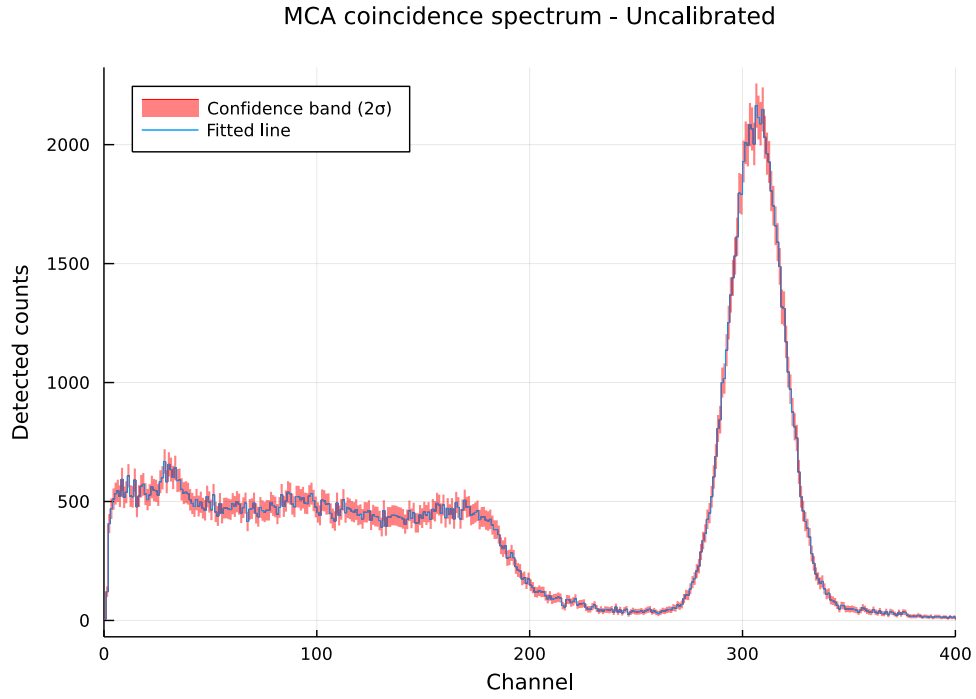


Figure 16: The uncalibrated MCA spectrum with coincidence plotted in a linear scale. Note the disappearance of swaths of structure, especially all structure following the first photopeak.

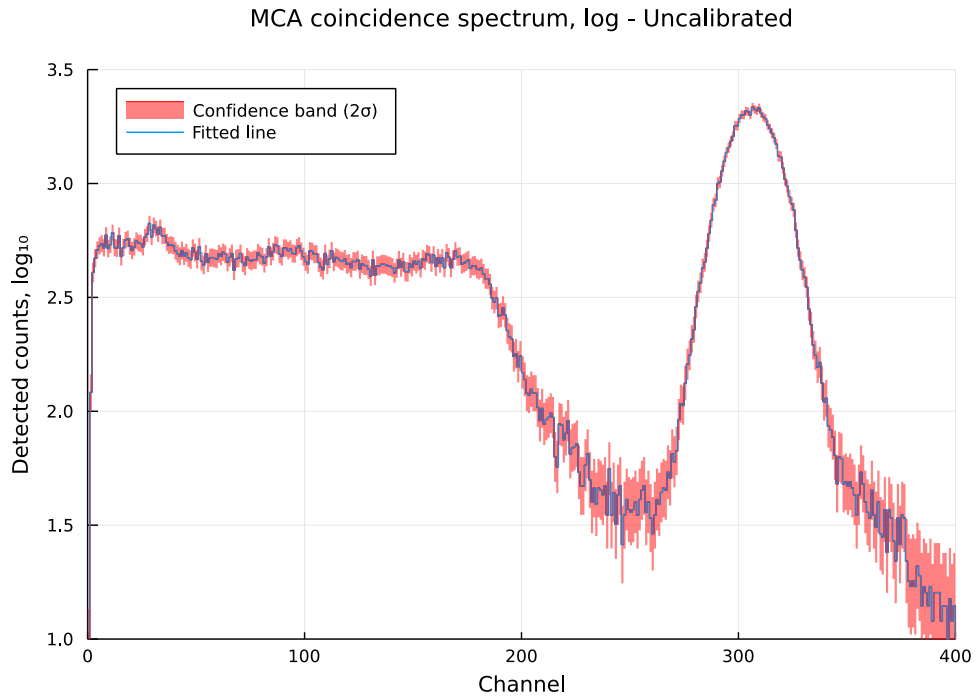


Figure 17: The same spectrum as before but plotted in log scale. Note how this gives the impression that the upper and lower errors on the data are different, but this is only due to the logarithmic scaling.

4 Discussion

4.1 Analysis of initial observations

4.1.1 More present line in spectrum

In the initial observations from figure 5 in both signals a ribbon surrounding a particular element of the signal has a stronger presence, meaning we have a higher rate of signals (events) in this area.

4.1.2 Fluorescence of NaI(Ti)

According to Leo [2], the re-emission process of a scintillator can in a first-order approximation be described by:

$$N = \frac{N_0}{\tau_d} \exp\left(-\frac{t}{\tau_d}\right) \quad (4)$$

Likewise, a more complete process which also describes the rise time of the PMT, the slow re-emission time, as well as a slower re-emission time can be described by the following equation:

$$V(t) = A \exp\left(-\frac{t}{\tau_{\text{slow}}}\right) + B \exp\left(-\frac{t}{\tau_{\text{fast}}}\right) - C \exp\left(-\frac{t}{\tau}\right) \quad (5)$$

In the above model, A , B , C are the amplitudes of the signal contributions. Additionally, τ_{slow} is the slow decay, τ_{fast} is the fast decay, and τ the rise time. Thus the terms from left to right will correspond to the slow and fast decays, and the rise time, respectively.

The typical fluorescence decay time will thus primarily be given by the fast fall time τ_{fast} (or τ_d in the case of the first-order approximation, equation (4)) [2]. To determine this value, a fit was performed with both models to the recorded data set. In figure 18 we have two fits, one for each of the above models ((4) & (5)). From the first fit, we extract a decay time of (378.5 ± 3.4) ns with the error in the first fit being extracted from the estimated covariance matrix. The second fit gives the value 274.35 ns. The error for the latter fit is the discussed in the next paragraph. To find the parameter the author employed bootstrap aggregation to find the uncertainties of the parameters. More specifically, this was done by fitting the models repeatedly to bootstrapped data, and recording the parameter values, from which the standard deviation was computed. This was combined with small perturbations in the initial parameters to also get a measure of the fits sensitivity to the parameters [9]. The data was sampled 10 000 times, which lead to the values for the second fit given in table 1.

A [mV]	τ_s [ns]	B [mV]	τ_f [ns]	C [mV]	τ [mV]
274.3 ± 43.3	298.3 ± 51.8	79.9 ± 0.9	4.11 ± 0.42	7074 ± 2878	36.7 ± 13.5

Table 1: The fit parameters for the LsqFit.jl fit together with the bootstrapped errors.

For the second fits, it is worthwhile discussing the algorithms used for calculating the errors on the fitted parameters. The problem to fit presented in equation (5) is a typical example of

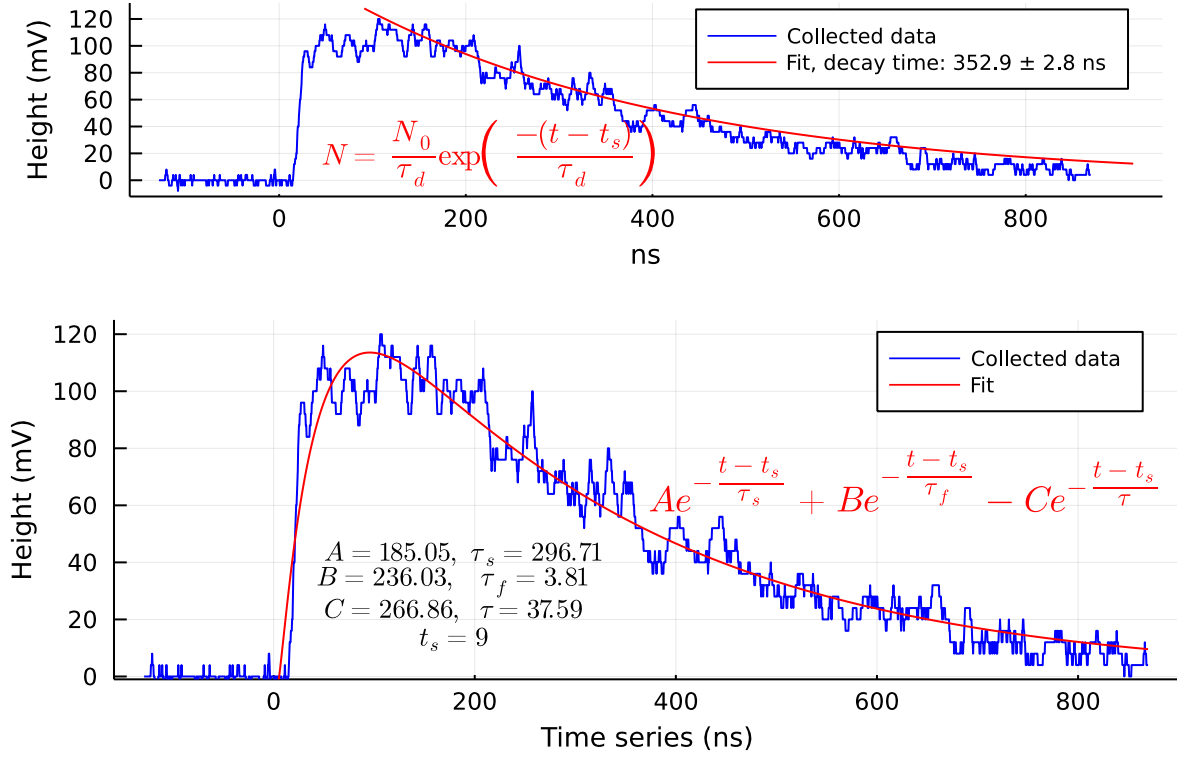


Figure 18: Fits to the dynode to extract decay time. For formulae, consult chapter 7 and 8 of [2].

a non-linear function and is notoriously difficult to fit [10]. This is usually done by estimating the inverse covariance matrix and then inverting it to find the covariance matrix². In the case of the second fit, the algorithm for extracting the covariance matrix failed using the implementation of Levenberg–Marquardt from the LsqFit.jl package [11], and could as such not estimate the errors directly. As such the fit was redone using the Python implementation of Minuit2, iminuit [12]. The result of this fit is displayed in 19.

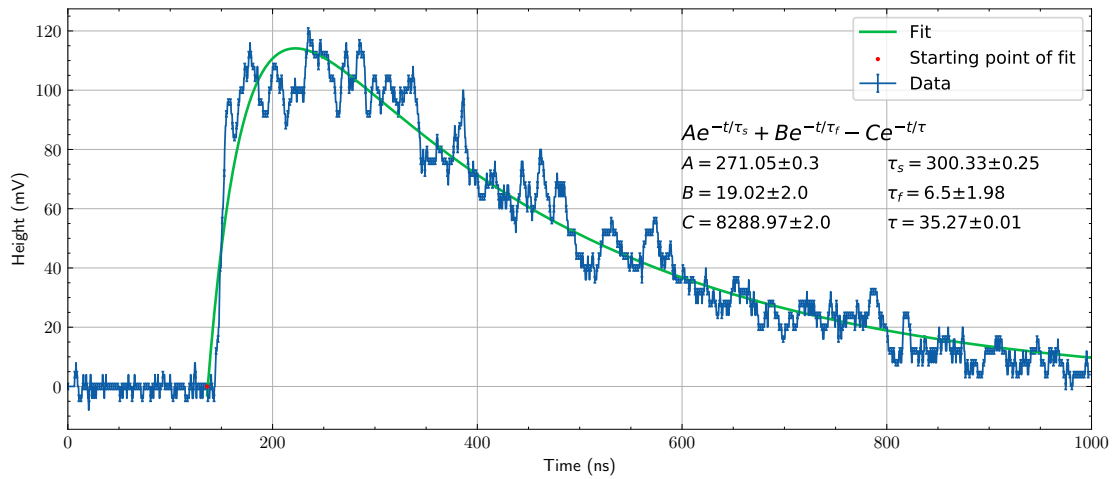


Figure 19: The iminuit fit to the dynode curve along with the spot marking where the fit is started for the two curves.

The values fits indicate a slower decay time of about (300 ± 40) ns, a faster decay at (6 ± 3) ns,

²A method of choice is often the Singular Value Decomposition (SVD)

and a rise time of circa (35.0 ± 1.5) ns.

The literature value for the slow decay time of a NaI(Tl) scintillator is about 230 ns [2], meaning it is within about 1.75σ . This is not very convincing but the signal at hand also exhibits a lot of noise, meaning that with an improved signal measurement and model (see later) a better value could possibly have been achieved. Depending on the age of the detector it is also possible that the scintillator simply takes longer to decay. The authors could not find any authoritative source of the fast decay. Regardless, the fitted values are small in relation to the slow decay times and thus have some internal consistency.

The rise times are larger than given in Leo, where the main component of the decay is given at about 230 ns. However, due to the age and use of the detector it could be that the rise time has become slower.

In the recorded data the signal did not start at zero, meaning one should compensate for this by including a time shift to the start of the signal.

$$-t \longrightarrow -(t - t_{\text{shift}})$$

Preceding the fitting procedure, the data was firstly shifted so the signal started about 0, and then the above t_{shift} was modified to fine-tune the start of the signal.

Note how this fit could not be done with the anode signal, as the anode signal already incorporates smoothing of the curve as well as additional amplification.

4.2 Working point of PMT

The working point of the PMT was chosen to be 850 V mostly based on how it was situated in the plot, being in the middle of the curve and seemingly being in a saddle point. Unfortunately, this value is quite close to the range where saturation starts to occur. The reason that this value was chosen nonetheless, is that the structure in the SCA spectrum was harder to recognize without increasing the voltage. The author was under the impression that this would indeed increase the quality of the data, but it may have been that it contributed more noise (extra counts) without being necessary as the important spectrum – done with the MCA module – can compensate for lower count-rates due to the long acquisition time.

One instance of this is that the noise increases with higher voltages, meaning that the discriminator will let through signals originating from the electronics instead of the source.

4.3 Manually integrated spectrum with SCA

The spectra in figure 14 were found by simply plotting the data with their Poisson errors. We expect these curves to give a rough estimate of the distribution of photon energies, where the LLD voltages combined with the window size gauges the interval of the energies which

contribute to the bin $[LLD, LLD + \Delta E]$. One should note that there also were constant positive displacement from zero of about 40 mV which was found by observing the SCA signal when the LLD was set to zero, meaning all values are slightly shifted when using the SCA.

In the left histogram noise may contribute to the leftmost peak, but an important implication of the displacement of the SCA, is that the initial peak close to zero most likely is *not* situated there. This indicates that it is more probable, that it is an additional structure of the spectrum which we at this stage are unable to resolve. From figure 2 an initial photopeak is identified between 0.4 and 0.6 V. The structure after the peak is not discernible in the left histogram, as well as the Compton edge.

Additionally, the step of the window of the SCA was not exact but also carried a small offset from the selected value. This is not hugely important, as the SCA spectra are complemented by a measurement with higher resolution and better binning exactness. In any case, this offset was very small, and could also have stemmed from the fact that the oscilloscope could not display differences / select points with arbitrary accuracy.

In the right histogram remaining features of the histogram can easily be identified with the theoretical contributions. The Compton edge is visible at around 0.2 V with a photopeak following it. The structure beyond this peak correspond to the expected contributions from the $^{22}\text{Ne}^* \longrightarrow ^{22}\text{Ne}$ transition with a photopeak at ~ 1.8 V and its Compton edge prior.

4.4 MCA without coincidence

4.4.1 Feature recognition

In figure 20 the energy spectrum with marked features is displayed. In the far left of the spectrum, the peak observed in the hand-made spectrum is indeed re-identified slightly displaced from zero. The exact nature of this peak will be discussed later in this section and again after energy calibration.

In the MCA spectrum the regimes carrying the theoretical features of the Compton edges and photopeaks are easily identifiable for both the 511 keV and 1275 keV emissions. Additional contributions which one can recognize are firstly a sharp peak at low energies, and a bump in the Compton continuum preceding the 511 keV-Compton edge. These will be identified and their character will be discussed after the energy calibration has been performed.

However, it is most probable that the bump corresponds to the backscattering of the photons. This as the energy of backscattered photons is close to the Compton edge energy while also not having a characteristic peak structure, as it is more broader regime where the scattering cross-section is increased.

With this in mind, the peak in the earlier part of the spectrum would come from some other mechanism in the source. The primary candidate for the peak in question would in that case

be the electron capture, but this will have to be determined on energy grounds.

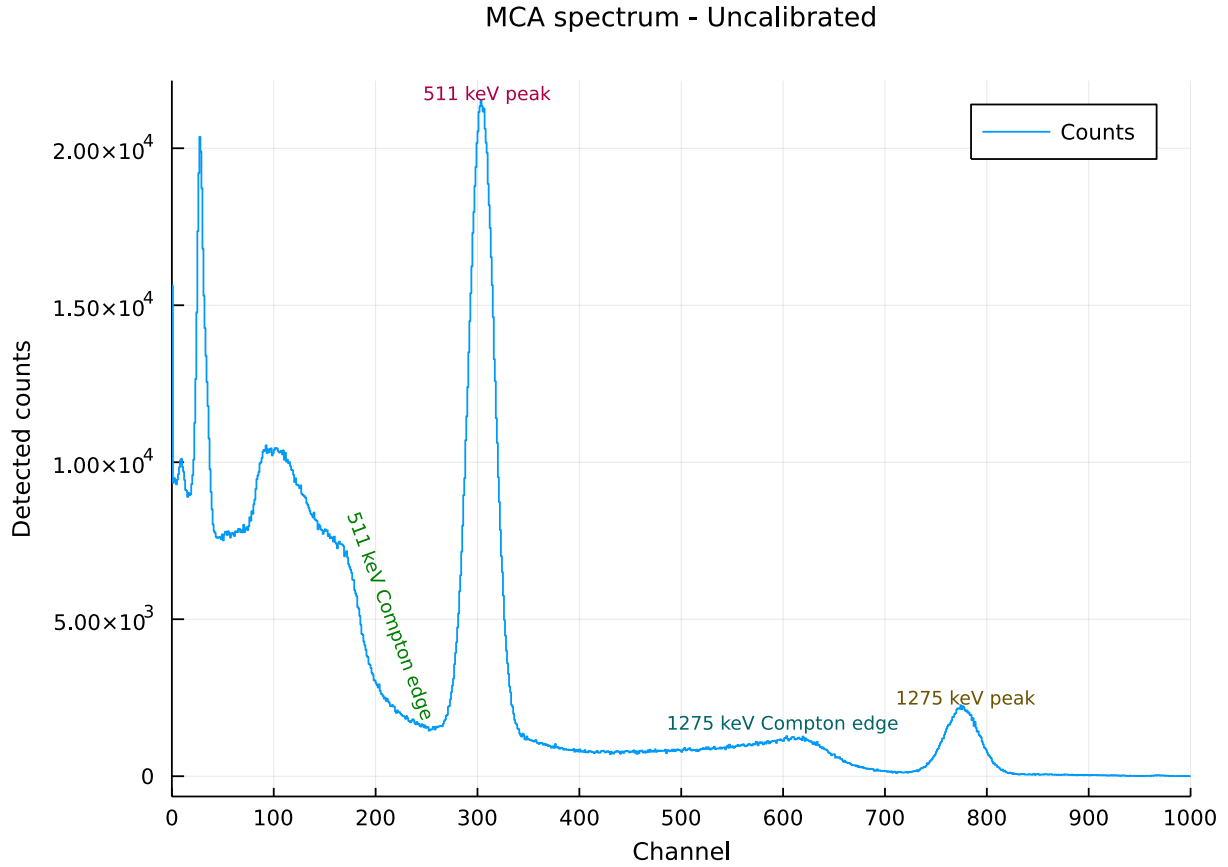


Figure 20: The uncalibrated but annotated MCA spectrum with the errors removed to make the plot less cluttered. The main features from the theoretical contributions are clearly shown with the two left bumps/peaks left to identify.

4.4.2 Feature fitting

For fitting the peaks a Gaussian with added terms accounting for noise is used:

$$N(x) = A \exp\left(-\frac{(x - \mu)^2}{2\sigma^2}\right) + a + bx \quad (6)$$

The noise terms can be selected depending on the region currently of interest. From these fits the energy resolution in the area can be found. For the 1275 keV peak, only a fit with a constant term was chosen, as we only expect a local noise contribution in the region stemming mainly from the equipment. In figure 21 this fit is displayed.

When fitting the 511 keV an additional linear term was considered for the contributions of the Compton edge of the higher energy peak. This is displayed in figure 22.

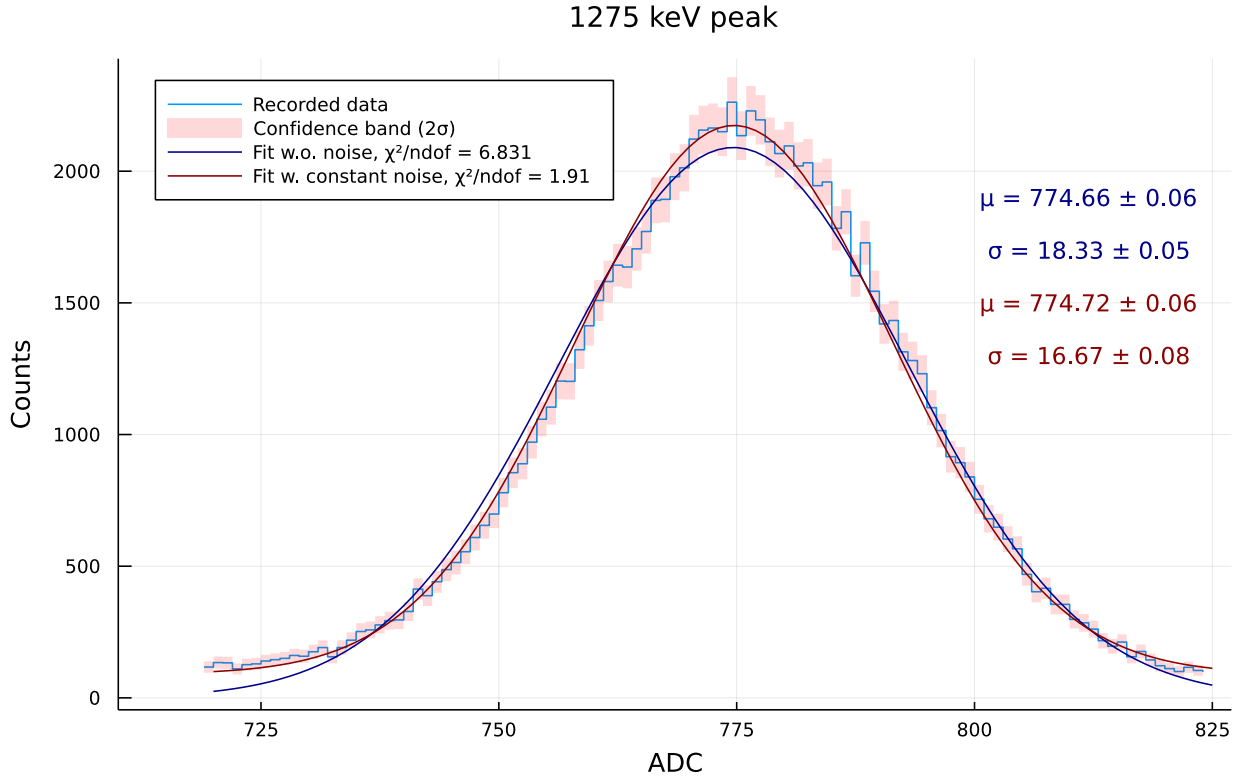


Figure 21: Two fits to the 1275 keV peak with the respective χ^2/ndof values given alongside the characteristic of the fit. On the right hand side the essential fitted parameters for the Gaussian are given.

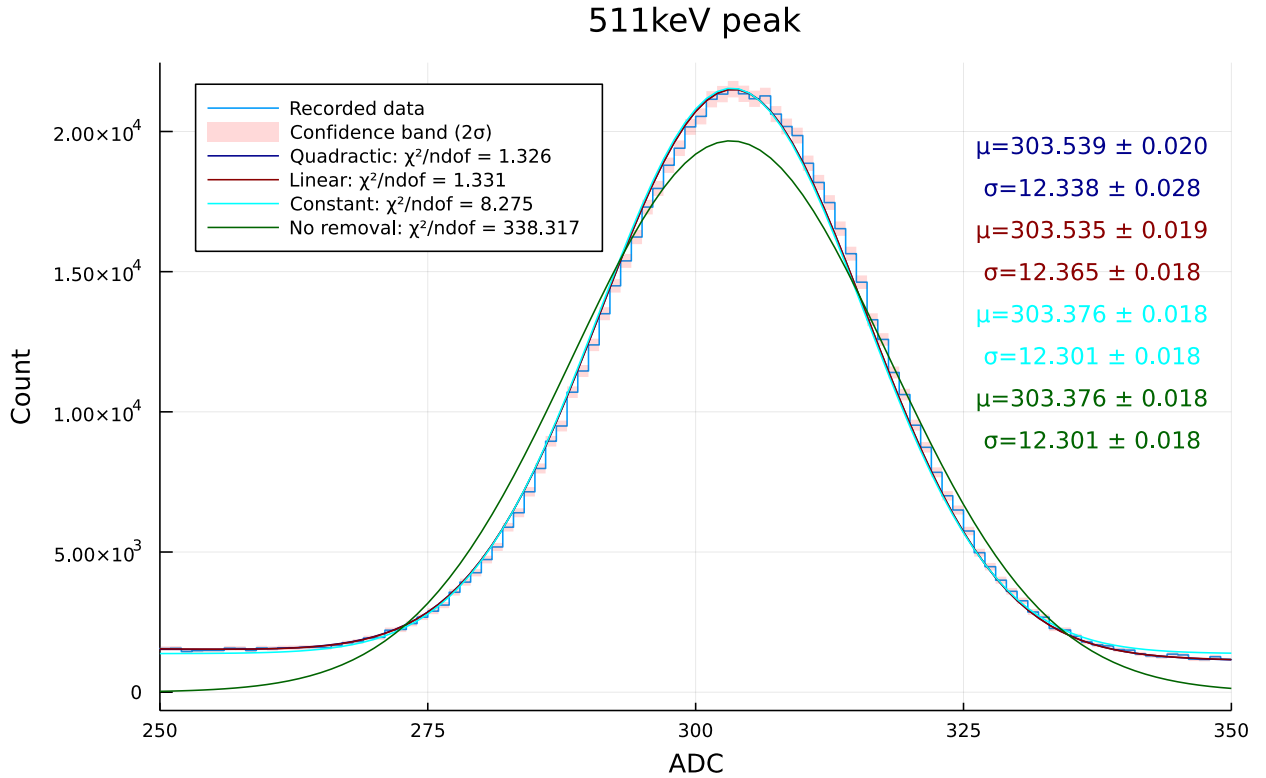


Figure 22: Several fits with different kinds of noise compensation for the photopeak at 511 keV. Again, the χ^2/ndof values are given along which kind of noise compensation is considered with the essential parameters color coded (and ordered) on the right side.

For the function to fit the Compton edge, the error function is chosen as the underlying model.

$$\text{erf } x = \frac{2}{\sqrt{\pi}} \int_0^x e^{-t^2} dt$$

However, we must consider that the height, width, and position may vary depending on the underlying distribution. Thus we choose the normal Gaussian as the underlying model which we then rewrite in terms of the standard error function.

$$N(x) = A \int_0^x \exp\left(-\left(\frac{x-\mu}{\sqrt{2}\sigma}\right)^2\right) dx \stackrel{t=\frac{x-\mu}{\sqrt{2}\sigma}}{=} B \int_0^{\frac{x-\mu}{\sqrt{2}\sigma}} e^{-t^2} dt = C \text{erf}\left(\frac{x-\mu}{\sqrt{2}\sigma}\right) \quad (7)$$

Where B absorbed the factor coming from the variable substitution while C accounts for the customary scaling of the error function. To this initial model linear noise is added to account for background.

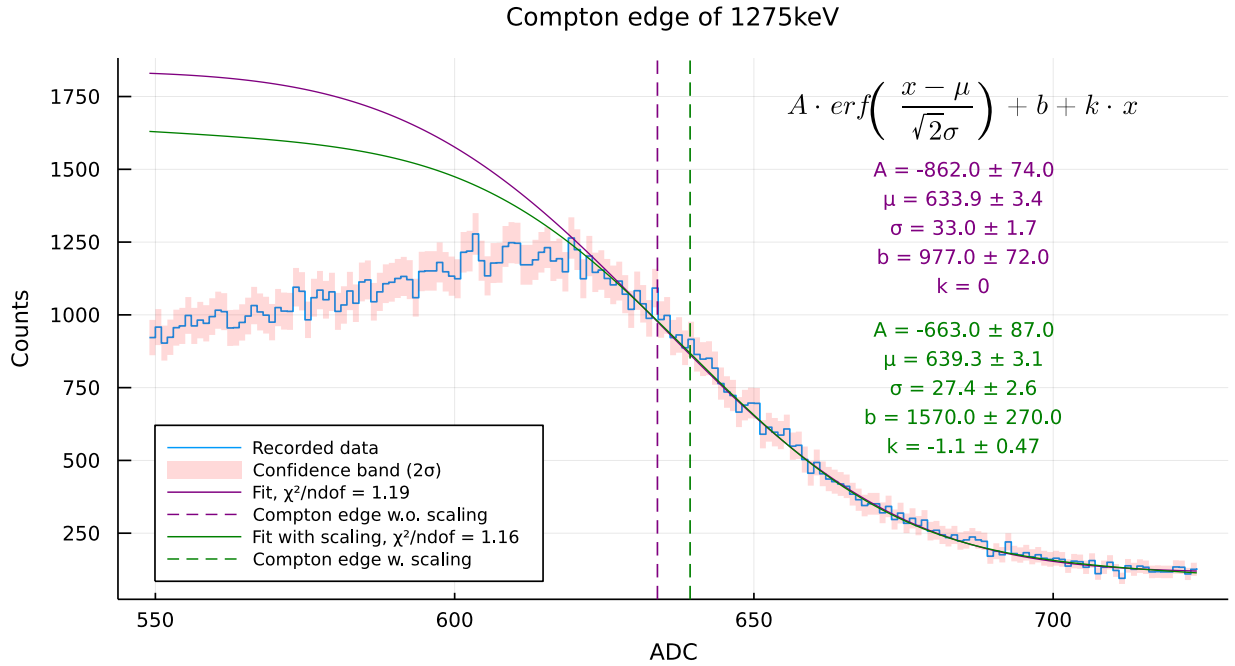


Figure 23: Two fits for the 1275 keV Compton edge, one with with constant noise removal and one with linear removal. Model and determined parameters from the fits with errors are included.

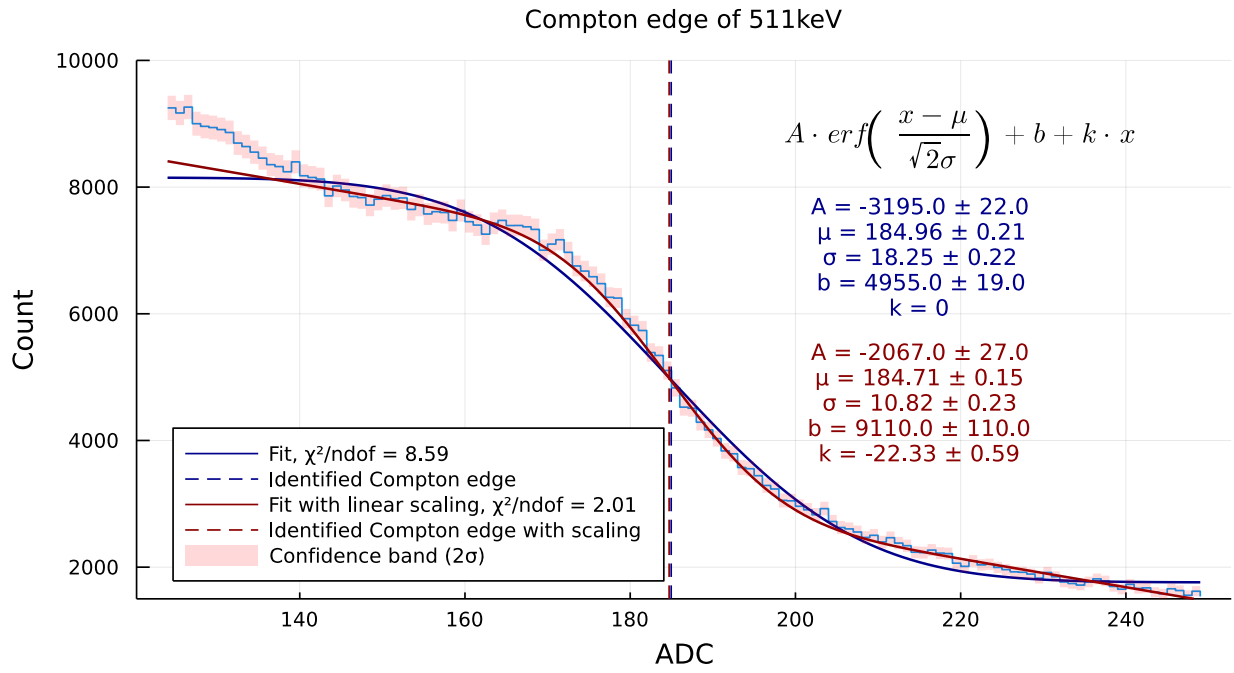


Figure 24: Two fits for the 511 keV Compton edge, one with with constant noise removal and one with linear removal. Model and determined parameters from the fits with errors are included.

4.4.3 Energy calibration

By fitting the theoretical positions of the features to the fitted values one can extract a formula for converting energy values to ADC channels. In figure 25 the result of two such fits are displayed, one with all points and one with only the first three.

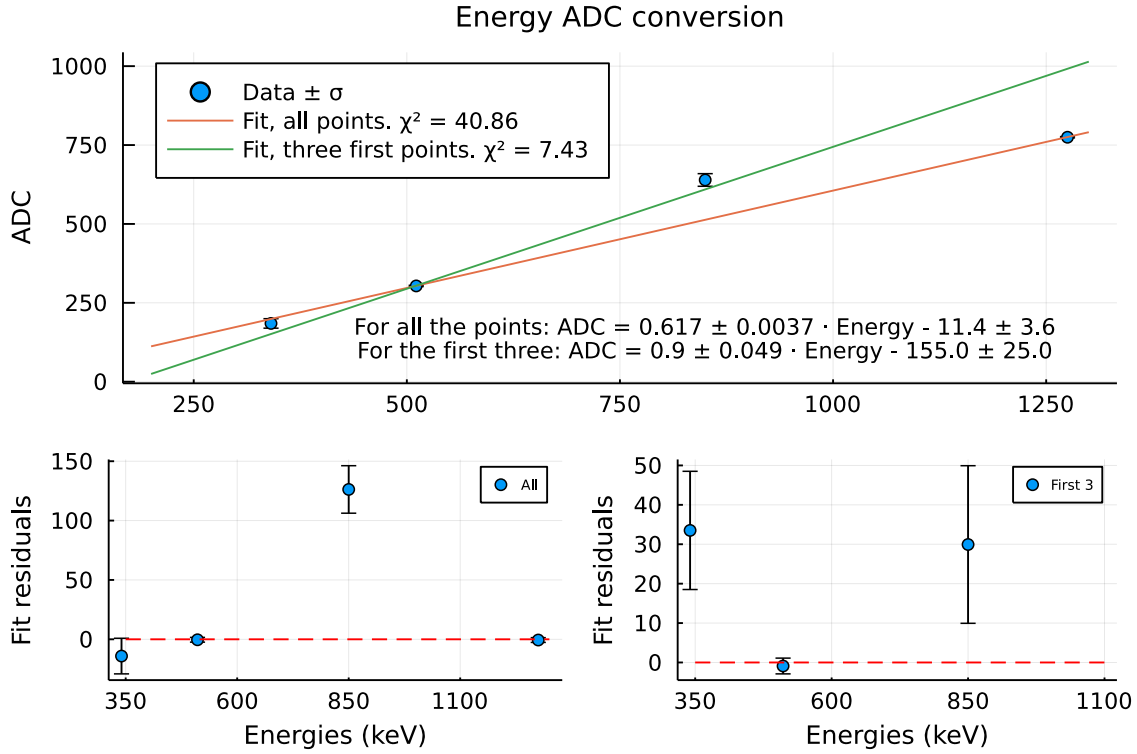


Figure 25: Linear fit to the calibration data together with the plotted residuals. Note how the third point is about 5σ from the expected mean of zero. In the upper plot the energy to ADC conversion is given. Note how this trivially also provides the means to convert the ADC spectra into energy spectra.

If the detector were perfectly linear, we expect a linear relationship. However, as one can see, the third point corresponding to the fit to the Compton edge at 850 keV is several standard deviations from line. That this point is weighted so little stems from the fact that the error in this fit was large in comparison to the other values. The pull plot can be seen in figure 26.

In any case, it seems that the detector does not display a linear behaviour. The problem can also not be easily remedied by improving the fit of the third point, as for it to appear in the expected voltage range from the fit would be impossible.

From the fitted peaks, we can now determine the energy resolution for the detector in the ranges by using equation 2. Performing the calculations for the two fitted peaks gives the resolutions given in table 2.

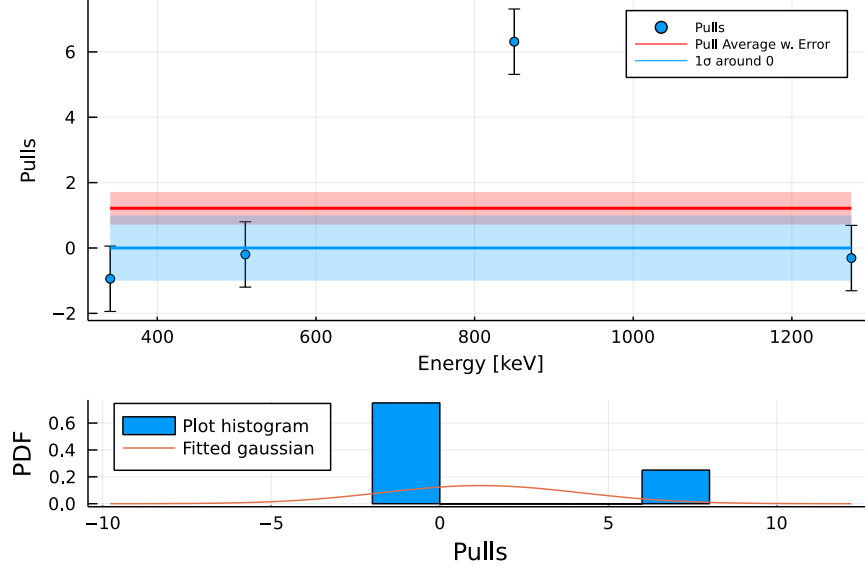


Figure 26: A plot of the pulls together with their mean with error. Note how the coincidence and localization of this the mean of the pulls and the value 0 ± 1 gives a measure of the quality of the fit. Again, the mean of the pulls is skewed about one sigma due to the abnormal value of the third point. Below, a Gaussian fit to the residuals are given. Note how the majority of the pulls are localized around 0 further indicating the quality of the fit would be high neglecting the third point.

Peak [keV]	Resolution
511	$(18.398 \pm 0.020) \times 10^{-2}$
1275	$(8.6770 \pm 0.0250) \times 10^{-2}$

Table 2: The energy resolution of the detector given for the two photopeaks. That the energy resolution is better at higher energies most probably stems from the fact that the amount of noise is reduced there. It could also be the case that the detector simply attenuates the signal less in this area.

4.4.4 Identification of lower peak and comparison with MCA without coincidence

In figure 27 the entire Compton continuum of the 511 keV. From this we can see that lowest peak is around 60 keV and the bump is at about 180 keV.

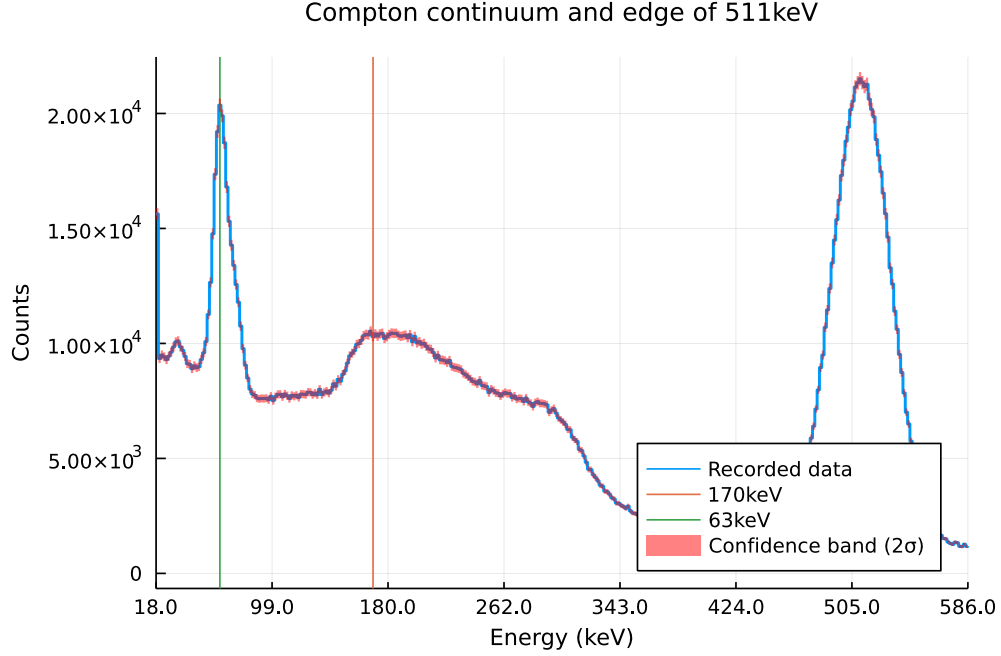


Figure 27: The calibrated MCA spectrum without coincidence.

Likewise in figure 28 a fit to the lowest peak is shown.

From the calibrated data the authors assumes the lower peak to come from some interaction with the lead shielding. Conceivably, it could be a characteristic X-ray from the lead. Indeed, the theoretical value for one such transition is 72 keV. The peak closer to the edge should stem from the backscattering process, which has a theoretical energy of the photon at 170 keV.

Both predicted sources' theoretical energies are offset from the recorded energies with a shift of about 10 keV, which probably stems from inaccurate calibration.

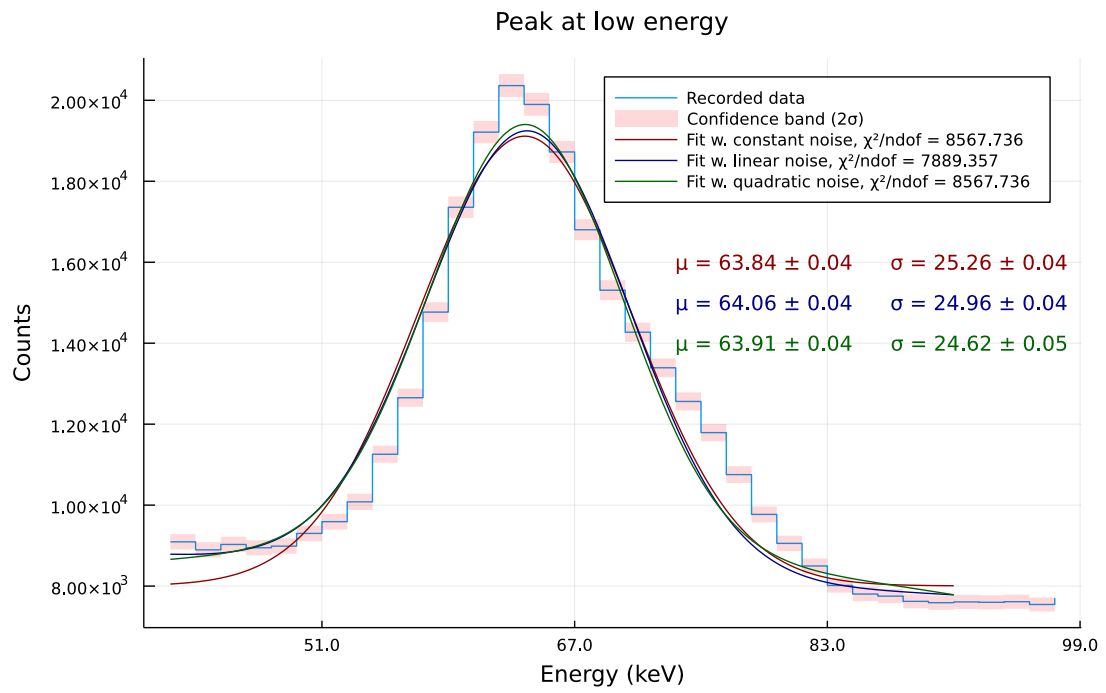


Figure 28: Three Gaussian fits to the lower energy. Note how this peak is distributed over fewer bins leading to higher uncertainty in the χ^2/dof values.

4.5 MCA spectrum with coincidence

The values recorded when recording with the coincidence gate along with the mean of these measurements can be found in table 3. The counts with coincidence accounts for a bit less than 30% for both PMTs, respectively. Indeed, when comparing with the upper bound for the counts derived in equation (3) one finds they are very close to the values recorded without coincidence.

Measurement	Coincidence	PMT1 On	PMT2 On
1	62.3	226.2	234.1
2	63.0	227.1	235.9
3	66.7	231.8	237.1
4	67.9	234.8	240.2
5	72.2	238.7	243.9
μ	66.41	231.72	238.24

Table 3: Some counts per second values for the two PMTs and the count for when the coincidence was turned on. Note with Poisson statistics how the counts for the two individual PMTs are about 1.3σ from another, giving about a 10% chance of them having the same mean. This means that there is a 90% change that some small parameter differentiates the two PMTs which might skew the coincidence counts.

This can either mean, that the attenuation in air and in the scintillator (short travel distances in the scintillator) are very small, or higher saturation may contribute to the counts via noise counts. The latter may be, but should in that case stem from the discriminator being poorly set, as the used voltage fit the predicted working point curve well.

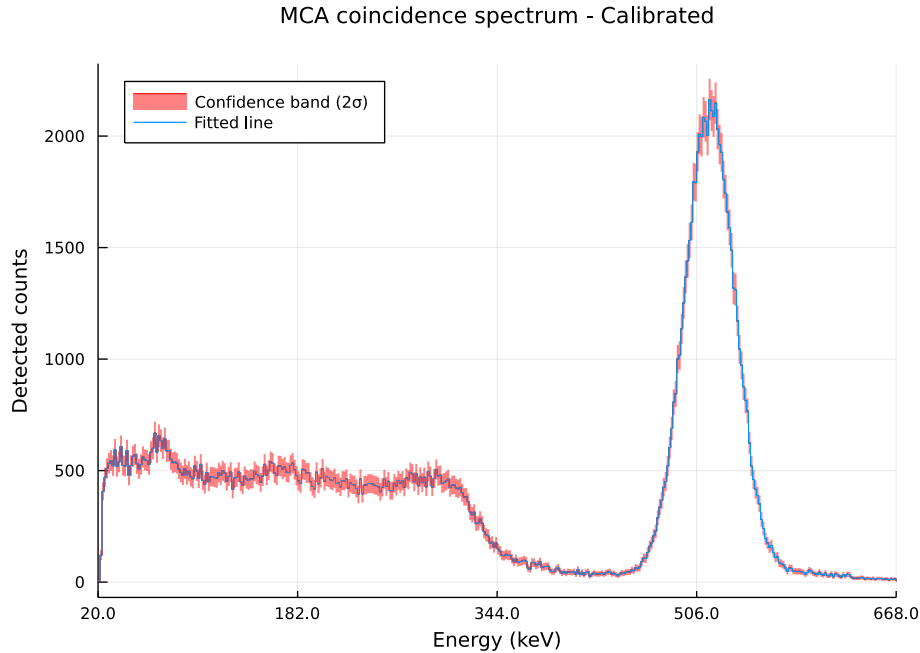


Figure 29: The calibrated MCA coincidence spectrum with errors. Note the low energy peak which still exhibits a certain additional amount of counts.

Finally, we compare the differences and similarities between the plot displayed in figure 29 and in figure 15. Importantly the overall counts are lower, this is to be expected as even

events which should appear in coincidence might not due to the detector resolution. Another important point is that the photopeak of course remains, but also the Compton edge. This is, however completely logical, as the interaction of photons from the $e^+ e^-$ annihilation with matter will also happen in coincidence a certain amount of the time. Most interesting is however the fact that a small part of the lowest peak is still there. This would indicate that the emission line at this point should also conserve some momentum or equivalent law to ensure that the emission can be recorded colinear. This is the main reason why the 1275 keV emission disappears when using coincidence; the chance of two such photons being emitted colinearly and simultaneously from the sample negligible.

In the case of an infinitely extended detector, many more counts would be observed here (and in general), as the decay could be observed from all angles. However, more significantly, an infinite detector would allow to distinguish spatial correlations between photons better, meaning the decay of o- P s would be able to be investigated.

5 Conclusion

In conclusion, the electron positron annihilation was investigated using some tools used in nuclear and particle physics. The decay time of the NaI(Tl) scintillator was determined to be about (300 ± 40) ns alongside its rise time of (35.0 ± 1.5) ns, giving a characterization of the scintillator used and indicating the aging of the scintillator might have degraded these aspects.

Subsequently, the saturation of the PMT was determined to start at a bias voltage about 910 V. Also the working point was determined giving a value of circa 850 V.

With this knowledge initial spectra were taken informing a MCA spectrum both with and without coincidence. From this the author can authoritatively state that the main features from the theoretical spectra were identified with relative errors of a few percent. Finally, the lower peak of the spectrum were determined to stem from x-rays from the decay of the source and the bump of the Compton continuum was identified as the backscattering from the interactions in matter.

A Safety considerations

A.1 The activity of the Na source

In the experiment we are using a ^{22}Na source which as explained in section 1 decays into ^{22}Ne and a positron. To protect the operator from abnormal doses of radiation, the source is enclosed in a lead chamber. It is contained in a 25 mm diameter plastic disk. When purchased in April 2009 the initial activity was (370.00 ± 0.05) kBq (the error here is estimated as such due to the professional fabrication of the source which should imply a high degree of accuracy in the activity). This particular isotope has a half-time of (2.601 ± 0.001) years [1].

The experiment was conducted in November 2021. The time difference between the acquisition of the source and the experiment date was as such about 12.5 ± 0.05 years. Using the exponential law:

$$N(t) = N_0 e^{-\lambda t}$$

with the half time $T_{1/2}$ being related to λ via: $T_{1/2} = \ln(2)/\lambda$ [2]. Plugging in our half-time we get:

$$N_{2021} = N_{2009} e^{-\lambda \ln 2 / T_{1/2}} = (13.21 \pm 0.18) \text{ kBq} \quad (8)$$

A.2 Protection by shielding

In general for beam-attenuation in a medium Beer-Lambert's law holds:

$$I = I_0 \exp \left[- \int \mu(x) dx \right] \quad (9)$$

Here I is the measured intensity of the beam after traveling a distance x in the material and $\mu(x)$ the linear attenuation coefficient. This is a measure of how much of the beam is scattered/absorbed per unit thickness in the material, with I being a measure of the absorbed intensity.

The rate of the source above calculated determined to be about 13.21 kBq. The energy of the emitted photons is smaller or equal to 1275 keV from the $^{22}\text{Ne}^* \longrightarrow ^{22}\text{Ne}$ transition. The density of lead is about $(11.340 \pm 0.005) \text{ g/cm}^3$ [1].

From the table of mass attenuation coefficients in [13], for 511 keV we have $\mu/\rho_{511} = (16.14 \pm 0.01) \times 10^{-2} \text{ cm}^2/\text{g}$, meaning $\mu_{511} = (183.03 \pm 0.01) \times 10^{-2} \text{ cm}^{-1}$. This is visualized in figure 30.

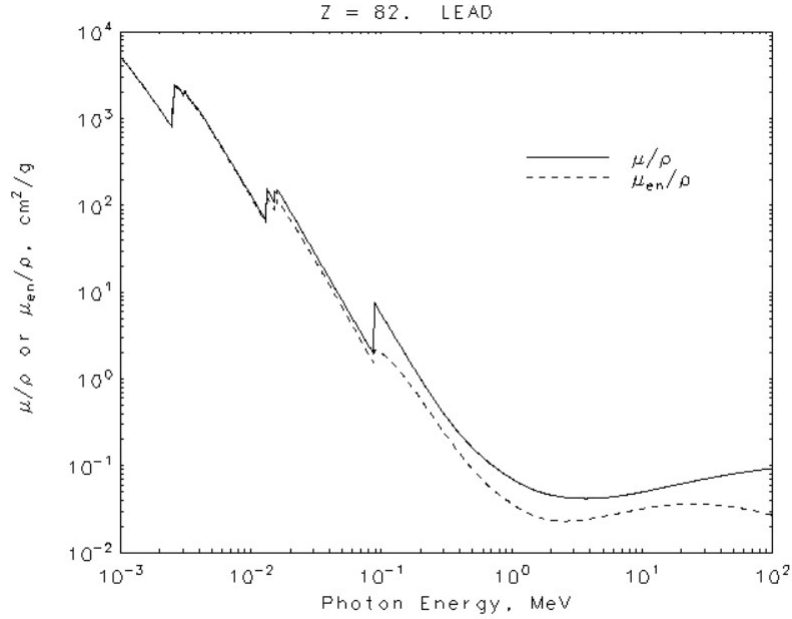


Figure 30: [13]

For the photon energy from the neon de-excitation the mass attenuation coefficient is not directly available, but can be extracted using a linear interpolation to be $\mu/\rho_{1275} = (5.81 \pm 0.01) \times 10^{-2} \text{ cm}^{-1}$, giving $\mu_{1275} = (6.59 \pm 0.57) \times 10^{-3} \text{ cm}^{-1}$.

With these combined facts we can formulate the Beer-Lambert law for the 511 keV γ -radiation penetrating 5 cm of lead shielding:

$$I = I_0 e^{-\mu \cdot x} = (1.401 \pm 0.001) \text{ Bq}$$

Here I_0 is the activity of the sample before the shielding as seen in equation (8) and μ as retrieved from [13].

If all the radiation had had the energy 1275 keV, the attenuation would give:

$$I = I_0 e^{-\mu \cdot x} = (12\,780.0 \pm 170.0) \text{ Bq}$$

Note that these account for a third of the decay results.

A.3 Average dose

The maximum dose limit in Switzerland for non exposed persons is about 1 mSv/year. The same regulation provides a table of the doses given for different isotopes. In the case of ^{22}Na its dose at 10 mm in tissue is $h_{10} = 0.33 \text{ (mSv/h)/GBq}$ [1].

Using a working distance of about 1 m and a total time in the lab of about 20 hours together with the calculated activity one gets a total dose $D \approx 87 \text{ nSv}$. This is way below the average dosage recommended per year.

For the shielded source using the activity resulting from Beer-Lambert's law one gets a dose $D_{S-511 \text{ keV}} \approx 9 \text{ pSv}$ as well as $D_{S-1275 \text{ keV}} \approx 84 \text{ nSv}$.

References

- [1] Aldo Antognini and Chiara Casella. e^+e^- annihilation experiment. https://vp.phys.ethz.ch/Experimente/pdf/Instructions_eplus_minus_2020.pdf. Accessed: 22.11.2021.
- [2] William R Leo. *Techniques for nuclear and particle physics experiments: a how-to approach*. Springer Science & Business Media, 2012.
- [3] David Griffiths. *Introduction to elementary particles*. John Wiley & Sons, 2020.
- [4] Charles Kittel. *Einführung in die Festkörperphysik*. Oldenbourg Wissenschaftsverlag, 2013. Original title: Introduction to solid state physics.
- [5] Louis Lyons. *Statistics for nuclear and particle physicists*. cambridge university press, 1989.
- [6] Roger J Barlow. *Statistics: A Guide to the Use of Statistical Methods in the Physical Sciences*, volume 29. John Wiley & Sons, 1993.
- [7] Mauro Donega. P1/P2 Data Analysis Toolbox FS 21, March 2021.
- [8] Wikipedia Foundation. Electrical termination.
- [9] Aurélien Géron. *Hands-on machine learning with Scikit-Learn, Keras, and TensorFlow: Concepts, tools, and techniques to build intelligent systems*. O'Reilly Media, 2019.
- [10] Alejandro L Garcia. *Numerical methods for physics, second edition, revised*. Prentice Hall Englewood Cliffs, NJ, 2000. More specifically chapter 5: "Analysis of Data", page 170.
- [11] John Myles White and Patrick Kofod Mogensen et al. LsqFit.jl, 2021. Available at: <https://github.com/JuliaNLSolvers/LsqFit.jl> accessed on 19.12.2021.
- [12] Hans Dembinski and Piti Ongmongkolkul et al. scikit-hep/iminuit, Dec 2020.
- [13] J. H. Hubbell and S.M Seltzer. Tables of x-ray mass attenuation coefficients and mass energy-absorption coefficients from 1 keV to 20 MeV for elements $z = 1$ to 92 and 48 additional substances of dosimetric interest*, 2004. More specifically, the entry for lead: <https://physics.nist.gov/PhysRefData/XrayMassCoef/ElemTab/z82.html>.